Title

Excess area dependent scaling behavior of nano-sized membrane tethers

Permalink

https://escholarship.org/uc/item/5118p45x

Authors

Ramakrishnan, N
Sreeja, KK
Roychoudhury, Arpita
et al.

Excess area dependent scaling behavior of nano-sized membrane tethers

N. Ramakrishnan[1], **K. K. Sreeja**[2], **Arpita Roychoudhury**[3], **David M. Eckmann**[1,4], **Portonovo S. Ayyaswamy**[5], **Tobias Baumgart**[6], **Thomas Pucadyil**[7], **Shivprasad Patil**[3], **Valerie M. Weaver**[8], and **Ravi Radhakrishnan**[1,2,9,*]

[1]Department of Bioengineering, University of Pennsylvania, Philadelphia, PA, 19104, USA

[2]Department of Chemical and Biomolecular engineering, University of Pennsylvania, Philadelphia, PA, 19104, USA

[3]Department of Physics, Indian Institute of Science Education and Research, Pune, 411008, India

[4]Department of Anesthesiology and Critical Care, University of Pennsylvania, Philadelphia, PA, 19104, USA

[5]Department of Mechanical engineering and Applied Mechanics, University of Pennsylvania, Philadelphia, PA, 19104, USA

[6]Department of Chemistry, University of Pennsylvania, Philadelphia, PA, 19104, USA

[7]Department of Biology, Indian Institute of Science Education and Research, Pune, 411008, India

[8]Department of Surgery and Anatomy, University of California San Francisco, San Francisco, CA, 94143, USA

[9]Department of Biochemistry and Biophysics, University of Pennsylvania, Philadelphia, PA, 19104, USA

Abstract

Thermal fluctuations in cell membranes manifest as an excess area $(\mathscr{A}_{\mathrm{ex}})$ which governs a multitude of physical process at the sub-micron scale. We present a theoretical framework, based on an in silico tether pulling method, which may be used to reliably estimate $\mathscr{A}_{\mathrm{ex}}$ in live cells. We perform our simulations in two different thermodynamic ensembles: (i) the constant projected area and (ii) the constant frame tension ensembles and show the equivalence of our results in the two. The tether forces estimated from our simulations compare well with our experimental measurements for tethers extracted from ruptured GUVs and HeLa cells. We demonstrate the significance and validity of our method by showing that all our calculations performed in the initial tether formation regime (i.e., when the length of the tether is comparable to its radius) along

---

[*] rradhak@seas.upenn.edu.

with experiments of tether extraction in 15 different cell types collapse onto two unified scaling relationships mapping tether force, tether radius, bending stiffness κ, and membrane tension σ. We show that $\mathcal{R}_{\mathrm{bead}}$ is an important determinant of the radius of the extracted tether, which is equal to the characteristic length $\xi = \sqrt{\kappa/2\sigma}$ for $\mathcal{R}_{\mathrm{bead}} < \xi$, and is equal to $\mathcal{R}_{\mathrm{bead}}$ for $\mathcal{R}_{\mathrm{bead}} > \xi$. We also find that the estimated excess area follows a linear scaling behavior that only depends on the true value of $\mathcal{A}_{\mathrm{ex}}$ for the membrane, based on which we propose a self-consistent technique to estimate the range of excess membrane areas in a cell.

Keywords

1. Introduction

The mechanical properties of a cell can be used as a surrogate marker to identify cellular phenotypes. Mechanical characterization has been particularly useful in identifying a number of pathophysiologies — well known examples include the stiffening of malaria infected erythrocytes and hepatocytes, the softening of metastatic cancer cells, and the sickle shape of an erythrocyte laden with hemoglobin S [1, 2, 3]. Several works in biomechanics have aimed to characterize cells based on mechanical measurements using a wide range of techniques such as flow and optical cytometry, manipulation using micropipette aspiration, optical tweezers and laser traps, and microfluidic devices (see [1, 4, 5] for comprehensive reviews). These studies have focused on whole cell measurements and hence have investigated the relationship between the mechanotype and pathophysiology at the cellular and tissue scales. In many cases, the changes in mechanical properties are primarily caused by variations in the structure and organization of the cellular cytoskeleton [6] and the extracellular matrix [7]. Such subcellular scale rearrangements can significantly impact not only the mechanical properties of the cell membrane but also can significantly impact geometrical properties such as cell membrane excess area at length-scales smaller than cellular dimensions (i.e., tens of nanometers to less than one micron).

This length scale under discussion significantly impacts the ability of the cell membrane as an effective organizer and a host for functional signaling complexes. For example, a bi-directional coupling can be established between the cell exterior and cell interior in a "geometry-dependent" fashion through the control of membrane excess area [8], because $\mathcal{A}_{\mathrm{ex}}$ is the conjugate variable for membrane tension as well as the membrane curvature. Several mechano-sensitive signaling events can therefore be transduced via the regulation in $\mathcal{A}_{\mathrm{ex}}$: they include cell-ECM interactions, which can tune acto-myosin tension and influence cell-proliferation through integrin-mediated signaling pathways [9, 10, 11]. Glycocalyx remodeling can influence membrane-curvature distribution on the cell surface and initiate a proliferative cell-response, funneling through integrin-mediating signals [12]. Cellular recycling pathways responsible for cargo transport from the endosome to the plasma membrane can also induce and nucleate cell-membrane protrusions providing dominant mechanisms for cell migration and motility [13, 14]. These examples serve to reiterate how

membrane excess area, in response to the tuning variables like tension, and by influencing the curvature distribution of the cell membrane, can transduce signals impacting cell-fate decisions.

The sub-cellular scale relevant to the above discussion corresponds to the dimensions primarily set by the cortical cytoskeletal mesh, which has been estimated to be between $l_c = 150 - 500$ nm [15, 16]. The mechanical properties of a patch of the cell membrane that spans the region between multiple cytoskeletal pinning points, with typical dimensions l_c, can differ from the bulk because the nature of the thermal undulations (and the associated conformational entropy of the membrane) depends directly on l_c, and in turn influences the system's free energy. We denote the size of the membrane patch as $\mathcal{L}_{\text{patch}}$. The total area of the membrane (denoted by $\mathcal{A}$) is in general larger than the projected area of the cytoskeletal mesh (denoted by $\mathcal{A}_{\text{patch}} = \mathcal{L}_{\text{patch}}^2$) [6, 17]. The characteristics of the membrane deformations and undulations can be described by a dimensionless scalar quantity called the membrane excess area given as $\mathcal{A}_{\text{ex}} = 100 * (\mathcal{A} - \mathcal{A}_{\text{patch}})/\mathcal{A}_{\text{patch}}$ and the membrane is taken to be flat when $\mathcal{A}_{\text{ex}} = 0$ and curved/ruffled if $\mathcal{A}_{\text{ex}} > 0$. The presence of excess area (and curvature gradients) can alter the local signaling microenvironment for a number of biophysical processes whose downstream components include curvature sensing proteins like BAR, Exo70, and ENTH domains [18, 19, 14]. Notable processes where modulations in the membrane excess area at the sub-cellular scale can significantly impact common cellular functions including intracellular transport of cargo or viral/bacterial internalization through exo-/endo-/phago-cytosis [20, 21], cell polarization [22, 23], and cell motility [24]. Hence it is logical to posit that the primary mechanisms linking the cell-microenvironment to cell fate can revolve around the physical factors impacting the membrane at length-scales below l_c [6, 25, 8, 12, 26].

We note that a number of experimental studies have focused on how membranous reservoirs respond to perturbations in the physical environment of the cell. The estimates for excess membrane area determined using conventional morphometric measurements, involving osmotic shock assays and cryo-EM [27] do not delineate thermally undulating excess areas, which causes a mis-estimation of the area. Moreover, such methods, by averaging over the entire cell (or even 100s of cells), ignore the heterogeneity on the scale of l_c at a single cell level or the asymmetry in membrane response that could exist in a polarized cell (where the basal and apical surfaces may sustain very different membrane properties). On other hand, tether pulling assays provide a powerful route to systematically study the various heterogeneities in the membrane surface [28, 29, 25, 30, 31, 32, 33, 34, 35], but their application to estimate membrane excess areas for all cell types is limited by the theoretical framework used for analysis. In this article, we propose a theoretical framework/ computational model applicable to tether pulling assays to obtain reliable estimates for the membrane excess area. Unique to our modelling approach is a new methodology that allows incorporation of large deformations as well as thermal membrane undulations in the estimate.

2. Computational model

We consider a fluctuating membrane bounded by a square frame of size $\mathcal{L}_{\mathrm{patch}} \sim l_c$. $\mathcal{A}$, $\mathcal{A}_{\mathrm{patch}}$, and $\mathcal{A}_{\mathrm{ex}}$ are respectively the curvilinear, projected, and excess areas of the membrane. This choice represents a model for membrane with finite $\mathcal{A}_{\mathrm{ex}}$ where the effect of the cytoskeleton is taken into account in a mean-field fashion. We note that more complex models of cytoskeletal interactions that explicit consider pinning have been reported [33, 36]. However, the mean field model we adopt here effectively captures the role of cytoskeletal pinning through the frame tension τ or the excess area $\mathcal{A}_{\mathrm{ex}}$; details of the model are given below. We discretize the membrane surface into a triangulated surface that contains M triangles intersecting at N vertices and forming L links [37, 38] and the statistical weights of the membrane conformations are governed by the discrete form of the Canham-Helfrich Hamiltonian [39, 40]:

$$\mathcal{H} = \underbrace{\sum_{i=1}^{N} \frac{\kappa}{2}(c_{1,i}+c_{2,i})^2}_{\text{bend}} + \underbrace{\sigma \mathcal{A} - \tau \mathcal{A}_{\mathrm{patch}}}_{\text{stretch}} + \underbrace{\frac{K_A}{2}(\mathcal{A} - \mathcal{A}_0)^2}_{\text{incompressibility}}. \tag{1}$$

κ and σ are respectively the bending rigidity and the bare surface tension of the membrane, while τ is the frame tension that represents the effect of the boundary frame. The surface tension is coupled to the membrane curvilinear area $\mathcal{A}$ while the frame tension is coupled to the projected area $\mathcal{A}_{\mathrm{patch}}$. $c_{1,i}$ and $c_{2,i}$ are the principal curvatures at a given vertex i computed as in our earlier work [41]. The area of the cell membrane obeys an incompressibility condition which is set by the area compressibility modulus K_A. In our studies we take $\sigma = 0$. However when thermal undulations are taken into account, the effective surface tension in the membrane will be non-zero due to renormalization effects and a mapping between the renormalized tension and excess area has been quantified in our earlier work [42].

The configurations of a planar membrane patch can be evolved under two different thermodynamic conditions namely: (i) the constant N-σ-τ-T ensemble and (ii) the constant $N-\sigma-\mathcal{A}_{\mathrm{patch}}-T$ ensemble. In the former we hold σ and τ as constants and this is equivalent to experimentally extracting tethers in a constant N-P-T setting. The constant N-σ-τ-T ensemble was previously described in reference [43]. Since $\mathcal{A}_{\mathrm{patch}}$ is a free variable in the N-σ-τ-T ensemble we constrain the value of $\mathcal{A}$ by setting $K_A = 4.1$ μN/m. On the other hand, in the constant $N-\sigma-\mathcal{A}_{\mathrm{patch}}-T$ - ensemble, in which we hold σ and $\mathcal{A}_{\mathrm{patch}}$ as constants, is extremely useful to systematically investigate the effect of $\mathcal{A}_{\mathrm{patch}}$ on the formation of membrane tethers. Since we fix $\mathcal{A}_{\mathrm{patch}}$ we allow for area fluctuations in the constant $N-\sigma-\mathcal{A}_{\mathrm{patch}}-T$ ensemble by setting $K_A = 0$.

The conformational states of the triangulated surface in both the constant N-σ-τ-T and $N-\sigma-\mathcal{A}_{\mathrm{patch}}-T$ ensembles are evolved using the dynamically triangulated Monte Carlo (MC) technique which consists of two independent MC moves: (i) *a vertex move* that simulates thermal fluctuations, (ii) *a link flip* that captures the fluid nature of biological

membranes. For simulations in the constant $N\text{-}\sigma\text{-}\tau\text{-}T$ ensemble we also introduce an additional MC move: *a boundary move* that allows for changes in $\mathscr{A}_{\text{patch}}$. Detailed information about the Monte Carlo techniques may be found in Suppl. Info., Sec. S1. A MC step consists of N vertex moves and L link flips that are performed at random and all the moves are accepted using the Metropolis scheme [44]. The boundary move is performed once in every 10 MC steps and is also accepted using the Metropolis scheme. All the simulations reported here have been performed using a membrane patch with $N = 2601$ vertices and the statistics are collected over 1.5 million MC steps following an equilibration run of the same duration.

For a given value of κ, σ and $\mathscr{A}$, the constant $N - \sigma - \mathscr{A}_{\text{patch}} - T$ and $N\text{-}\sigma\text{-}\tau\text{-}T$ ensembles can be uniquely mapped from one to the other through the membrane excess area $\mathscr{A}_{\text{ex}}$. This is demonstrated in Figure 1 where we have shown $\mathscr{A}_{\text{ex}}$ as a function of $\mathscr{A}$, in the constant $N\text{-}\sigma\text{-}\tau\text{-}T$ ensemble, for five different values of the frame tension $\tau = -412, -206, 0, 206$ and 412 μN/m. The range of τ was chosen to correspond with experimentally measured cortical tension values in mammalian cells, for a review see Sens and Plastino [17]. It may be seen that $\mathscr{A}_{\text{ex}}$ has a unique value for every τ which decreases with increasing frame tension. Furthermore, $\mathscr{A}_{\text{ex}}$ is an intrinsic variable that only depends on τ and is independent of and $\mathscr{A}$ and $\mathscr{A}_{\text{patch}}$, both of which are extrinsic variables. This result clearly demonstrates the equivalence of the constant $N - \sigma - \mathscr{A}_{\text{patch}} - T$ and $N\text{-}\sigma\text{-}\tau\text{-}T$ ensembles. The data shown in Figure 1 corresponds to a membrane with $\kappa = 20\ k_{\text{B}} T$ and $\sigma = 0$ while similar results for $\kappa = 40, 160\ k_{\text{B}} T$ may be found in Suppl. Info., Sec. S2.

2.1. Analytical model for the membrane excess area

The excess area of a planar membrane in the small deformation limit ($|\nabla h| \ll 1$, where h denotes the height of the membrane surface, measured with respect to the xy plane) can be analytically estimated to be [45, 46];

$$\mathscr{G} = \frac{100}{2\mathscr{L}_{\text{patch}}^2} \sum_{q=q_{\text{min}}}^{q=q_{\text{max}}} \frac{k_{\text{B}} T}{\kappa q^2 + \sigma}, \quad (2)$$

where q denotes the wavenumber of all possible undulation modes in the membrane and k_{B} the Boltzmann constant. The effect of the frame tension τ does not enters into Equation (2) since it only contributes to the mode $q = 0$. The maximum value of the wavenumber $q_{\text{max}} = 2\pi a_0^{-1}$ is set by the size of the triangulated vertices a_0 while its minimum value $q_{\text{min}} = 2\pi l_p^{-1}$ is set by the length scale l_p with $l_p \gg a_0$ and $l_p \quad \mathscr{L}_{\text{patch}}$. We have performed all our analysis using three values of $l_p = 150, 250,$ and 510 nm that represent the variations in the cytoskeletal length-scales. We note that this model only has applicability in the regime of small $\mathscr{A}_{\text{ex}}$ when $|\nabla h| \ll 1$ is satisfied and is expected to fail in regimes where the $\mathscr{A}_{\text{ex}}$ of the cell is not small (see Suppl. Info., Sec. S3 and S4).

2.2. In silico tether pulling assay

If $\mathscr{F}_t$ be the force required to extract a tether of radius $\mathscr{R}_t$ and length l_t from the membrane patch, as illustrated in Figure 2, the total energy $\mathscr{H}_{tot}$, which has a contribution due to membrane deformations (Equation (1)) and an additional part from the work done to extract the tether (assuming that the tether is a perfect cylinder and ignoring thermal undulations), is given by [47]:

$$\mathscr{H}_{tot} = \frac{\kappa \pi l_t}{\mathscr{R}_t} + 2\pi \sigma l_t \mathscr{R}_t - \mathscr{F}_t l_t. \qquad (3)$$

Minimization of the total energy with respect to l_t and $\mathscr{R}_t$ yields: (i) $\kappa = \mathscr{F}_t \mathscr{R}_t / (2\pi)$ and (ii) $\sigma = \mathscr{F}_t / (4\pi \mathscr{R}_t)$. These relationships allow one to determine the elastic properties of the cell membrane through tether pulling experiments; however, the non-trivial geometry of a tether (which in general is not a perfect cylinder) and the underlying membrane patch (which is not a perfect planar entity but rather a ruffled surface subject to undulations, especially under high $\mathscr{A}_{ex}$) limits the applicability of Equation (3). To overcome these limitations, we have extended the umbrella sampling technique [48] to extract tethers of a specified length $\mathscr{L}_t$ from a membrane in the $N - \sigma - \mathscr{A}_{patch} - T$ ensemble. This is analogous to tether extraction in experiments where a constant outward force is applied on a selected region of the cell membrane through an AFM or an optical tweezer. In our model, we include a harmonic biasing potential of the form $\mathscr{H}_{bias} = k_{bias}(l_t - \mathscr{L}_t)^2/2$ to Equation (1), per standard practice in umbrella sampling simulations. Here k_{bias} is the spring constant of the biasing potential and $\mathscr{L}_t$ is a reaction coordinate that denotes the prescribed length of the extruded tether. We performed umbrella sampling simulations at different values of $\mathscr{L}_t$ and collected the biased tether length distribution, $\mathscr{P}_b(l_t)$; the window size for umbrella sampling simulations were chosen such that $\mathscr{P}_b(l_t)$ in successive windows overlap. The unbiased or equilibrium distribution of the tether length, $\mathscr{P}_u(l_t)$, was computed from $\mathscr{P}_b(l_t)$ using the Weighted Histogram Analysis method (WHAM) [49, 50], which in turn was used to compute the potential of mean force for tether extraction as $\mathscr{W}_t(l_t) = -k_B T \ln \mathscr{P}_u(l_t)$. In all our calculations we took $k_{bias} = 2.05$ mN/nm^2 and this value was chosen so that the undulation modes of the membrane remains unaltered.

The length of the tether l_t is defined using a macroscopic order parameter, determined from two different sets of vertices $\{X_T\}$ and $\{X_B\}$, that are shown in Figure 2(a). $\mathbf{R}_T$ and $\mathbf{R}_B$, which are also shown in Figure 2(a), represent the centers of mass of the chosen vertices that define the two macroscopic variables from which the instantaneous tether length is calculated as $l_t = |\mathbf{R}_T - \mathbf{R}_B|$. While $\{X_T\}$ is predetermined at the start of the simulation, $\{X_B\}$ is computed at runtime and taken to be the set of all vertices at the boundary of the membrane patch (also see Suppl. Info., Sec. S10).

In a typical tether pulling assay, the bead used to extract the tether non-specifically binds to the membrane. To reflect this we choose the biased vertices in the tip to be a circular region of radius $\mathscr{R}_{bead}$; this is illustrated in Suppl. Info., Sec. S5. Since the non-specific binding does not control for the adhesive contact area, we vary the size of $\mathscr{R}_{bead}$ in our simulations.

The equilibrium configuration of a membrane patch with $\kappa = 20\ k_B T$ and $\mathscr{A}_{ex}{=}40\%$ is shown in Figure 2(a). The representative conformations of the membrane tether stabilized for an imposed tether length of $l_t{=}400$ nm in the constant $N{-}\sigma{-}\mathscr{A}_{patch}{-}T$ and $N\text{-}\sigma\text{-}\tau\text{-}T$ ensembles are shown in Figure 2(b) and (c), respectively. It may be noted that simulations in both these ensembles yield identical tether conformations, which once again point to the equivalence of the two.

2.3. Potential of mean force

For a given membrane patch, independent simulations are performed to extract tethers within a given umbrella sampling window. For all simulations reported in this article, we use at least 64 windows each of width 5 nm — the number of windows required to extract fully developed tethers increases with increasing $\mathscr{A}_{ex}$. Histograms of the instantaneous tether length in each of the windows are recorded for 1.5 million Monte Carlo steps and these statistics are converted to a potential of mean force (PMF) using the Weighted Histogram Analysis method [50]. The typical runtime for an umbrella-sampling window to sample 1.5 million MCS is around 36 hours on a 2.6 GHz processor.

2.4. Computing the radius and length of membrane tethers

The radius and length of the membrane tether $\mathscr{R}_t$ and l_t, respectively, can be determined exactly in the simulations, as shown in Figure 2(b). Let $[\mathbf{r}]$ be the set of all N_c vertices on the tubular region and $\mathbf{r}_{CM} = (N_c)^{-1} \Sigma_i \mathbf{r}_i$ their center of mass: here $\mathbf{r}_i$ is the three-dimensional position vector of vertex i in the Cartesian coordinates. The center of mass can be used to construct the gyration tensor as, $\mathbf{G}{=}(N_c)^{-1}\sum_{i=1}^{N_c}(\mathbf{r}_i - \mathbf{r}_{CM}) \otimes (\mathbf{r}_i - \mathbf{r}_{CM})$ whose eigenvalues are λ_1, λ_2, and λ_3. Since the tethers formed are axi-symmetric we identify λ_2 and λ_3 using the relation $\lambda_2 \approx \lambda_3$. Of the three eigenvalues, λ_1 represents the length of the tether, with $l_t \approx 2\sqrt{\lambda_1}$, and $\sqrt{\lambda_2}$ and $\sqrt{\lambda_3}$ represent its two principal radii. We estimate the average tether radius as $\mathscr{R}_t{=}(\sqrt{\lambda_2}+\sqrt{\lambda_3})/2$.

3. Experimental Methods

3.1. Cell culture

HeLa cells were placed in 35 mm petridishes at 37° C in 5% CO_2 in DMEM (Dulbecco's Modified Eagle's medium, Lonza) containing 10% FBS (Fetal Bovine Serum, Gibco) and 0.02% Penicillin/Streptomycin for 48 hours before commencing the experiment. A confluent culture of HeLa cells was treated with 0.25% Trypsin-EDTA (Gibco), detrypsinised in DMEM containing 10% FBS and seeded at a density of 80, 000 cells/coverslip (Ted Pella Inc., Redding), so that a single monolayer of cells are obtained on the coverslip.

3.2. Giant Unilamellar Vesicles (GUVs)

For the preparation of vesicles, 1, 2-dioleolyl-sn-glycero-3-phosphocholine (DOPC), 1, 2-dioleolyl-sn-glycero-3-phospho-L-serine (DOPS) (Avanti Polar, Alabaster, AL) and 1, 2-dioleolyl-sn-glycero-3-phospho-ethanolamine-N-(lissamine rhodamine B sulfonyl)(RhPE) (Invitrogen) stock solutions in chloroform, at room temperature were used. The lipid mix

was aliquoted in a glass vial to a total lipid concentration of 1 mM at a ratio of DOPC:DOPS:RhPE (84:15:1 mol%).

Gel-assisted formation of GUVs were carried out using polyvinyl alcohol (PVA) as described earlier [51], with a few modifications as per the requirements of the experiments. In this method of GUV formation, a drop of 5% w/v degassed PVA (MW 145, 000, Sigma) in deionized water is added to a clean glass coverslip placed on a hot plate set at $75°$ C. The water gets evaporated in about 10 minutes leaving a dry thin film of PVA on the coverslip. To this, around 3 μL of the 1 mM lipid stock solution in chloroform was added to dry PVA while on the hot plate to let the chloroform evaporate. The thin film was peeled off and immersed in eppendorfs containing 20 mM HEPES, 150 mM NaCl, pH 7.4 with 100 mM sucrose. This immersed film was left undisturbed for around one hour followed by gentle tapping to release the GUVs from the PVA film to the buffer solution. The buffer containing large free floating GUVs (10-15 μm) was pipetted out and used for tether pulling experiments.

3.3. AFM Experiments

AFM-based force spectroscopic experiments were performed using Nanowizard II atomic force microscope (JPK Instruments). The AFM liquid cell was assembled with freshly cleaved mica discs prior to adding the GUV solution. The liquid cell was then mounted on the AFM stage and left undisturbed for 20 minutes to allow the vesicles to settle on the mica surface. Using a fluorescence microscope attached with the AFM set up, we could confirm that the GUVs settled on the surface and the floating ones were washed away by exchanging buffer solution with HBS. Subsequently, the GUVs got ruptured on the mica surface and they were imaged using AFM. The images obtained using AFM revealed the location and height of the ruptured GUV patches which matched with that of the height of a single bilayer membrane (5-6 nm). Force spectroscopy was then performed on these particular patches to pull membrane tethers. Silicon nitride cantilevers (MikroMasch CSC38/AlBS) were used for pulling the tethers. Cantilevers were calibrated before each experiment and its spring constant was determined using equipartition theorem [52]. The measured spring constant of the cantilevers used for most experiments was found to be range of 20-80 mN/m. Constant speed mode was used for approaching the tip to the sample surface followed by retraction at the same speed. The approach-retract cycle was repeated at various points on the membrane patch using force mapping tool built in Nanowizard II software and force-displacement curves were recorded. Force curves showing step profiles were selected and analyzed using JPK data processing software by fitting the curves with the in-built functions to measure the force minimum corresponding to the tether force and step heights in retraction force curves.

4. Results

4.1. Extraction of membrane tether proceeds through three distinct regimes

We first demonstrate the characteristics of a tether extracted from a model membrane with κ = 20 $k_B T$ and $\mathscr{A}_{ex} \sim 40\%$, using a bead size of $\mathcal{R}_{bead}$ = 50 nm in the $N - \sigma - \mathscr{A}_{patch} - T$ ensemble. The tether is extracted using the umbrella sampling technique described in the

methods section, for reaction coordinate (imposed tether length) values in the range $0 < \mathcal{L}_t < 500$ nm, with a window size of 5 nm. The top panel in Figure 3 shows representative snapshots of the membrane stabilized at four different values of $\mathcal{L}_t = 0$, 200, 300, and 450 nm. At small values of $\mathcal{L}_t$, the membrane conformations show large undulations whose magnitudes are set by the value of $\mathscr{A}_{ex}$. However, at large values of $\mathcal{L}_t$, the membrane undulations are absorbed into the large out of plane protrusions that resemble a tether extracted from a planar membrane. It is noted that the shape of a fully developed tether (i.e., when the undulations in the planar region becomes very small) is consistent with that predicted for nearly planar membranes, using analytical methods [31, 53].

The instantaneous length and radius of the tether region, denoted by l_t and $\mathcal{R}_t$, as a function of the reaction coordinate $\mathcal{L}_t$, are shown in the middle and lower panels of Figure 3, respectively. Both l_t and $\mathcal{R}_t$ show non-monotonic behaviors with respect to $\mathcal{L}_t$, which are solely attributable to the non-zero excess area of the membrane. For membrane with thermal undulations, and hence non-zero excess areas, we identify three characteristic regimes for tether growth which are marked as shaded regions in the figure. These regions are characterized as follows:

- **Regime 1** ($l_t \approx \mathcal{R}_t$): for $\mathcal{L}_t < 75$ nm, where the tether radius and length are similar, the applied biasing potential only serves to suppress the short wavelength undulations in the membrane. This is reflected in the fact that the membrane conformations in this regime are not distinguishable from their equilibrium counterparts.

- **Regime 2** ($l_t \approx$ constant and $\mathcal{R}_t \propto \mathcal{L}_t^{-1}$): for $75 < \mathcal{L}_t < 300$ nm a pronounced protrusion is seen in the vicinity of the region where the biasing potential is applied. The radius of this protrusion decreases with increasing $\mathcal{L}_t$, while its length remains unchanged.

- **Regime 3** ($\mathcal{R}_t \approx$ constant and $l_t \propto \mathcal{L}_t$): for $\mathcal{L}_t > 300$ nm in Figure 3, the tether radius remains constant while its length increases linearly with $\mathcal{L}_t$, marking a region of tether growth. The linear increase in l_t fails to hold when all excess area in the membrane is drawn into the tether region.

The extent of the three regimes, depend on the values of κ and $\mathscr{A}_{ex}$. This is shown in the Suppl. Info., Sec. S6, where we have displayed the effects of $\mathscr{A}_{ex}$ and κ on the radius of the extracted tether. In conventional tether pulling experiments only regime 3 is well resolved, while regimes 1 and 2 are not commonly observed since these experiments do not have the required spatial resolution, as in our simulations, to resolve these regimes.

The characteristic length scale for a membrane, given by $\xi = \sqrt{\kappa/2\sigma}$ [54, 55], sets the limit below which curvature contributions are dominant. In our model, ξ is an increasing function of κ and $\mathscr{A}_{ex}$ — the latter may be deduced from the inverse relationship between σ and $\mathscr{A}_{ex}$ in Equation (2). In a tether pulling experiment performed in the $N - \sigma - \mathscr{A}_{patch} - T$ ensemble, the radius of the extracted tether depends either on ξ or on the size of the biased region $\mathcal{R}_{bead}$ used for tether extraction. This is shown in Figure 4 where we display the values of $\mathcal{R}_t$ as a function of $\mathcal{R}_{bead}$, for $\kappa = 20$, 40, and 160 $k_B T$ and $\mathscr{A}_{ex} = 10$ and 40%. The

conformations shown in panel (a) for a membrane with $\kappa = 20\ k_B T$ and $\mathscr{A}_{ex} \sim 10\%$, for $\mathcal{L}_t = 300$ nm, illustrates the interplay between the characteristic clearly length ξ and the imposed length $\mathcal{R}_{bead}$. While we observe fully grown and geometrically identical tethers for $\mathcal{R}_{bead}$ 75 nm, we find the tether extracted with $\mathcal{R}_{bead} = 100$ nm to be significantly different. A fully grown tether for this regime is only obtained at a much larger value of $\mathcal{L}_t$. The radius of a fully grown tether is also a strong function of $\mathcal{R}_{bead}$ and this feature is quantified in Figure 4(b) where we find the nearly constant tether radius ($\mathcal{R}_t \sim 80$ nm) for $\mathcal{R}_{bead}$ 75 nm to show a marked increase to $\mathcal{R}_t \sim 110$ nm when $\mathcal{R}_{bead} = 100$ nm.

In panels (b) and (c) of Figure 4 two key features are worth noting: (i) as expected, the value of $\mathcal{R}_t$ is an increasing function of κ for all values of $\mathcal{R}_{bead}$, and (ii) the dependence of $\mathcal{R}_t$ on $\mathcal{R}_{bead}$ is minimal for large values of κ and also when $\mathscr{A}_{ex}$ is large.

4.2. PMF and tether force

The PMF ($\mathscr{W}_t$) to extract a tether of length l_t from a membrane patch of fixed $\mathscr{A}_{ex}$ is computed from the umbrella sampling data using the WHAM technique (see methods section). $\mathscr{W}_t$ for a membrane with $\kappa = 20\ k_B T$ and $\mathscr{A}_{ex} \sim 40\%$ is shown in the top panel of Figure 5(a). The three characteristic regimes seen for $\mathcal{R}_t$ (see Sec. Figure 4.1) are also reflected in the form of $\mathscr{W}_t$. Here, we again observe three scaling regimes : (i) an initial linear regime given by $\mathscr{F}_1 l_t$, (ii) a second non-linear regime, $\propto l_t^2$, and (iii) a final linear regime, $\propto \mathscr{F}_2 l_t$. Both the linear regimes are shown as solid lines in panel (a) of Figure 5 and the latter is attributable to tether extrusion at a constant radius, for which the elastic energy is expected to scale as $\mathcal{H}_{tot} \propto l_t$ (Equation (3)). On the other hand, the source of the non-linear scaling is attributed to $\mathcal{R}_t$ being a decreasing function of l_t. We note that the scaling behavior is universal and is observed for all systems investigated.

The force required to extract the tether may be computed as $\mathscr{F}_t = \nabla_{l_t} \mathscr{W}_t$ where ∇_{l_t} denotes a gradient with respect to l_t. $\mathscr{F}_t$ can be estimated either from direct numerical differentiation of $\mathscr{W}_t$ or from the scaling relations — for the latter, $\mathscr{F}_t = \mathscr{F}_1$ in regime 1 and $\mathscr{F}_t = \mathscr{F}_2$ in regime 3. The tether forces computed using the two methods for $\mathscr{W}_t$ in Figure 5(a) are shown in the lower panel — symbols and lines correspond to $\mathscr{F}_t$ obtained using numerical differentiation and using the scaling relations, respectively. We find the estimates from both the methods to be in excellent agreement. Since direct numerical differentiation is subject to a large noise to signal ratio, we primarily rely on the scaling relation based method to estimate $\mathscr{F}_t$. As in experiments, we report the value of the force in the second regime as the tether force, i.e., $\mathscr{F}_t \sim \mathscr{F}_2$.

The tether force shown in Figure 5(a) has the same qualitative and quantitative behavior as that normally observed in experiments. The top and bottom panels in Figure 5(b) show forces required to extrude a tether from ruptured GUVs on mica and from HeLa cells, respectively — the tether extraction protocol is described in Suppl. Info., Sec. S7. The pulling speeds in both the experimental assays are taken to be 1 μm/s, which satisfies the assumption of quasi-equilibrium tether extraction employed in our simulations. Measurements at speeds less than that reported here are not possible due to the noise arising from cantilever thermal drift. Though there are no known techniques to calculate the precise

value of $\mathscr{A}_{\text{ex}}$ for both systems, it is reasonable to assume that it is finite. Similarly, there are no reliable experimental methods to measure $\mathscr{R}_{\text{bead}}$, but given that the AFM tip-membrane interactions are non-specific in nature it is reasonable to assume that $\mathscr{R}_{\text{bead}} < \xi$.

While the force-displacement curves for both the systems depend on the properties of their respective bilayer membrane, in the case of HeLa cells there may be additional contributions due to the underlying cytoskeletal mesh. Though we would expect ruptured GUVs on a mica surface to be free of any pinning contacts, there could be a finite number of pinning sites due to the chemical heterogeneity on the surface in spite of the surface being atomically smooth. The salt concentration in the buffer may screen the interactions between the membrane and the mica surface leading to a sparse contact between the two and the effect of these non-specific contacts on the force-displacement curves are minimal. The forces measured in experiments match very well with the numerically computed values of $\mathscr{F}_{\text{t}}$. The measured tether force is about 20 pN for tethers pulled from both the ruptured GUVs and the HeLa cells. For the case of ruptured GUVs, the tether length at which we observe a transition to the tether extrusion regime is consistent with that seen in our simulations, while that for the cells is considerably higher extending into few microns. We attribute this deviation to the lack of a suitable reference frame for cellular measurements.

As noted in the introduction, the size of the cytoskeletal mesh (l_c) bounding the cell membrane significantly influences the characteristics of the extracted tether. The current theoretical model only considers tethers from a homogeneous membrane with constant κ and $\mathscr{A}_{\text{ex}}$. However, to zeroth order, the role of the cytoskeleton in suppressing long wavelength undulations beyond l_c can be taken into account in our model by examining the dependence on the membrane patch size $\mathscr{L}_{\text{patch}}$. In Figure 6, we investigate this effect by extracting tethers from two planar patches with $\mathscr{L}_{\text{patch}} = 510$ nm and $\mathscr{L}_{\text{patch}} = 1.02$ μm, which are representative of cell membranes scaffolded by dense and sparse cytoskeletal meshes, respectively. Panels (a) and (b) show data for membranes with $\kappa = 20$ and 40 $k_{\text{B}}T$, respectively, for excess areas $\mathscr{A}_{\text{ex}}=10$ and 40%. It is evident from these figures that the PMF, and hence $\mathscr{F}_{\text{t}}$ and $\mathscr{R}_{\text{t}}$, in addition to the elastic parameters κ and $\mathscr{A}_{\text{ex}}$, are also functions of $\mathscr{L}_{\text{patch}}$. This points to the fact the cell may have a heterogeneous mechanical microenvironment depending on the cytoskeletal mesh size and may provide varied response to biochemical processes, such as nanocarrier or viral binding, depending of the characteristic value of l_c at the site of the process [36]. Hence, characterizing the mechanical properties of the cell membrane at the scale of l_c would be extremely important. In the following, we will only focus on membrane patches with $\mathscr{L}_{\text{patch}} = 510$ nm to establish how the excess area of the membrane can be inferred from tether pulling experiments.

It may be seen from Figure 6 that there are some subtle differences in the scaling behavior of the potential of mean force, $\mathscr{W}_{\text{t}}$, for small values of l_t. The slope $\mathscr{F}_1$ which characterizes the initial linear regime can either be positive or negative depending on the values of κ and $\mathscr{A}_{\text{ex}}$. For instance, in Figure 6(b), the initial regime of $\mathscr{W}_{\text{t}}$ for $\kappa = 40$ $k_{\text{B}}T$ and $\mathscr{L}_{\text{patch}} = 510$ nm has a positive slope for $\mathscr{A}_{\text{ex}}=10\%$ and a negative slope for $\mathscr{A}_{\text{ex}}=40\%$. This can be understood by analyzing the value of the reaction coordinate of the membrane in its equilibrium state (i.e., at $\mathscr{L}_{\text{t}} = 0$), which we denote as l_{t}^{eq}. This would correspond to the position of the minimum of

$\mathscr{W}_{\mathrm{t}}$. For systems with $l_{\mathrm{t}}^{\mathrm{eq}} \sim 0$, the tether length l_{t} increases with increasing imposed tether length $\mathscr{L}_{\mathrm{t}}$, and as a result the potential of mean force $\mathscr{W}_{\mathrm{t}}$ increases linearly with a positive slope. On the other hand, for systems with $l_{\mathrm{t}}^{\mathrm{eq}} > 0$, the tether length first decreases in the regime $\mathscr{L}_{\mathrm{t}} < l_{\mathrm{t}}^{\mathrm{eq}}$ and increases for $\mathscr{L}_{\mathrm{t}} > l_{\mathrm{t}}^{\mathrm{eq}}$ Since we always expect the position of the minimum of $\mathscr{W}_{\mathrm{t}}$ to be at $l_{\mathrm{t}}^{\mathrm{eq}}$, systems with $l_{\mathrm{t}}^{\mathrm{eq}} > 0$ would have a negative slope in the initial regime. This is characteristic of systems with large κ and $\mathscr{A}_{\mathrm{ex}}$, in which the curved morphologies of their native state [42] endow them with non-zero values of $l_{\mathrm{t}}^{\mathrm{eq}}$. We observe negative slopes in the initial regime for $\mathscr{W}_{\mathrm{t}}$ computed both in the constant $N - \sigma - \mathscr{A}_{\mathrm{patch}} - T$ and N-σ-τ-T ensembles, as is shown in Figures 7, 8 and 9.

The dependence of $\mathscr{W}_{\mathrm{t}}$ on the size of the membrane patch is also seen in our simulations in the constant N-σ-τ-T ensemble. We extracted tethers from four different membrane patches that have similar excess areas but have different $\mathscr{A}$ and $\mathscr{A}_{\mathrm{patch}}$; here we initialized the systems as described in Suppl. Info., Sec. S11 and membrane patches with different $\mathscr{A}$ were generated by changing $\mathscr{A}_0$, as described in Equation (1). The parameters for all the patches were taken to be $\kappa = 20\ k_{\mathrm{B}}T$, $\tau = 0$ and $\mathscr{R}_{\mathrm{bead}} = 50$ nm. In Figures 7 (a), (b), (c), where the four systems are marked A1-A4, we show the corresponding values of $\mathscr{A}$, $\mathscr{A}_{\mathrm{patch}}$, and $\mathscr{A}_{\mathrm{ex}}$ as a function of the imposed tether length $\mathscr{L}_{\mathrm{t}}$. Even at very large values of $\mathscr{L}_{\mathrm{t}}$ we only observe ~5% decrease in the value of $\mathscr{A}_{\mathrm{patch}}$ which in turn leads to a similar increase in $\mathscr{A}_{\mathrm{ex}}$ (see Figures 7 (b) and (c)). For all practical purposes, we can treat the membrane to have a nearly constant value of $\mathscr{A}_{\mathrm{ex}}$.

Figure 7 (d) shows the length and radius of the extracted tethers and as expected tether formation does not depend $\mathscr{A}$ and $\mathscr{A}_{\mathrm{patch}}$ but only on the membrane excess area. Similarly, the potential of mean force and the tether forces $\mathscr{F}_{\mathrm{t}}$, that are displayed in Figures 7 (e) and (f), show a strong dependence on the membrane area $\mathscr{A}$. As in Figure 6, we find both $\mathscr{W}_{\mathrm{t}}$ and $\mathscr{F}_{\mathrm{t}}$ to be decreasing functions of $\mathscr{A}$. The observed reduction in $\mathscr{W}_{\mathrm{t}}$ and $\mathscr{F}_{\mathrm{t}}$ may be explained as follows. $\mathscr{R}_{\mathrm{t}}$, the radius of a fully grown tether only depends on the elastic parameters as $\max\left(\sqrt{\kappa/2\sigma}, \mathscr{R}_{\mathrm{bead}}\right)$, while its length l_{t} is proportional to the degree of undulations in the membrane, i.e., l_{t} is proportional to $\mathscr{A}_{\mathrm{ex}}$. For a given $\mathscr{A}_{\mathrm{ex}}$, since the amount of material stored in the form of undulations increases with increasing $\mathscr{A}$, the threshold length for tether growth without any elastic deformations is significantly higher for large membrane patches. Hence, tether growth in large membrane patches proceeds primarily through ironing out of thermal undulations, which requires smaller energy, compared to tether growth in smaller membrane patches in which higher energy elastic deformations dominate.

4.3. Comparison of tether characteristics in the constant $N - \sigma - \mathscr{A}_{\mathrm{patch}} - T$ and N-σ-τ-T ensembles

We had so far qualitatively established that tether extraction in both the constant $N - \sigma - \mathscr{A}_{\mathrm{patch}} - T$ and N-σ-τ-T ensembles yield similar results. Here we make a quantitative comparison of (i) $\mathscr{R}_{\mathrm{t}}$ (ii) l_{t} (iii) $\mathscr{W}_{\mathrm{t}}$ and (iv) $\mathscr{F}_{\mathrm{t}}$ for tether extracted in the two ensembles for a membrane with $\kappa = 20\ k_{\mathrm{B}}T$ and $\mathscr{A}_{\mathrm{ex}} \sim 40\%$. The N-σ-τ-T simulations were performed with $\tau = 0$. The curvilinear area $\mathscr{A}$, projected area $\mathscr{A}_{\mathrm{patch}}$, and the excess area $\mathscr{A}_{\mathrm{ex}}$ of the membrane

patches in the two ensembles can be found in the Suppl. Info., Sec. S8. Though the values of $\mathscr{A}$ and $\mathscr{A}_{\text{patch}}$ are different for both these systems they have similar excess areas ($\sim$44% for the $N-\sigma-\mathscr{A}_{\text{patch}}-T$ ensemble and $\sim$42% for the N-σ-τ-T ensemble).

In Figure 8(a), we compare the measured values of $\mathscr{R}_t$ and l_t as a function of $\mathscr{L}_t$ for tethers extracted using the two thermodynamic ensembles of interest. As noted before for the constant $N-\sigma-\mathscr{A}_{\text{patch}}-T$ ensemble (see Figure 3) tether formation in the constant N-σ-τ-T ensemble also proceeds through three distinct regimes. The measured values of $\mathscr{R}_t$ and l_t display excellent quantitative agreement with their corresponding values measured in the constant $N-\sigma-\mathscr{A}_{\text{patch}}-T$ ensemble.

The potentials of mean force $\mathscr{W}_t$ for both systems, displayed in Figure 8(b), agree well for later values of l_t but have different slopes at small l_t, for the reasons mentioned in our discussions on Figure 6. On the other hand, the tether forces $\mathscr{F}_t$ computed in the two ensembles show excellent qualitative and quantitative agreement, and this is displayed in Figure 8(c). These results categorically show that the choice of the thermodynamic ensemble should not influence our results. Therefore, all of our subsequent studies were performed in the constant $N-\sigma-\mathscr{A}_{\text{patch}}-T$ ensemble.

4.4. Tether radii and forces measured in silico compare well with range of values measured in in vivo experiments

Pontes et. al. [56] have recently reported results for *in vivo* tether pulling assays studies of 15 different cell types in the central nervous system (CNS) — the data is also shown in the Suppl. Info., Sec. S9. Based on this study, we classify cells in the CNS into four distinct categories: (i) small κ ($20 - 60 k_B T$) & small σ, (ii) small κ & large σ, (iii) large κ (~ 160 $k_B T$) & small σ, and (iv) large κ & large σ. In order to establish the quantitative accuracy of our model, we compute the values of $\mathscr{R}_t$ and $\mathscr{F}_t$ for six model systems which are representative of the cells in the CNS. They are denoted by M1 ($\kappa = 20\ k_B T$, $\mathscr{A}_{\text{ex}} \sim 10\%$), M2 ($\kappa = 20\ k_B T$, $\mathscr{A}_{\text{ex}} \sim 44\%$), M3 ($\kappa = 40\ k_B T$, $\mathscr{A}_{\text{ex}} \sim 9\%$), M4 ($\kappa = 40\ k_B T$, $\mathscr{A}_{\text{ex}} \sim 43\%$), M5 ($\kappa = 160\ k_B T$, $\mathscr{A}_{\text{ex}} \sim 13\%$), and M6 ($\kappa = 160\ k_B T$, $\mathscr{A}_{\text{ex}} \sim 38\%$). These model systems are also depicted in Figure 9(a).

For each of the six model systems (M$_i$, with $i = 1 \cdots 6$), we extracted tethers using three bead sizes, chosen to be $\mathscr{R}_{\text{bead}} = 25$, 50, and 75 nm. We denote each set of data as M$_{ij}$, where j=1, 2, and 3 is the index for the three bead radii, respectively. The PMFs for these systems are displayed in Figure 9(b) and the presence of the three characteristic regimes for $\mathscr{W}_t$, discussed earlier, are evident. Despite a similarity in the scaling behavior, the values of $\mathscr{W}_t$ are highly sensitive to changes in both $\mathscr{R}_{\text{bead}}$ and the elastic parameters κ and $\mathscr{A}_{\text{ex}}$, predominantly so for the latter. The average values of $\mathscr{R}_t$ and $\mathscr{F}_t$ for the model systems are displayed in Figure 9(c) and (d) respectively. $\mathscr{R}_t$ is found to be independent of $\mathscr{R}_{\text{bead}}$ and, as expected, we find: (i) for a given κ, $\mathscr{R}_t$ is a decreasing function of $\mathscr{A}_{\text{ex}}$ (e.g. M1>M2), and (ii) for a fixed $\mathscr{A}_{\text{ex}}$, $\mathscr{R}_t$ is an increasing function of κ (e.g. M5>M3>M1). The tether force also shows a similar behavior, with $\mathscr{F}_t$ being larger for systems with smaller $\mathscr{A}_{\text{ex}}$ and larger κ. The range of values for the tether force ($10 < \mathscr{F}_t < 50$ pN) and radius ($60 < \mathscr{R}_t < 110$ nm) measured in our simulations compare very well with the experiments of Pontes et. al. [56],

where they report values in the range $15 < \mathcal{F}_t < 70$ pN and $43 < \mathcal{R}_t < 158$ nm. The large error bars seen for some systems are reflective of the rough free energy landscape for tether extraction under the prescribed conditions. This establishes the validity of our present model as a tool for interpreting tether pulling assays that aim to probe tethers in the nanoscopic scale.

Our results in Figure 10(a) and (b), depict the adherence to the constitutive relations derived by minimizing Equation (3). Briefly, the effective bending rigidity and the surface tension are expected as follow the relations $\kappa/a = (2\pi)^{-1}$ and $\sigma/\Gamma = (4\pi)^{-1}$, respectively. Here the scaling parameters are $a = \mathcal{F}_t \mathcal{R}_t / k_B T$ and $\Gamma = \mathcal{F}_t / \mathcal{R}_t$. As can be seen from the figures, data from both our simulations (marked M1–M6 and shown as open symbols) and from the experiments of Pontes et. al. [56] (marked C1–C15 and shown as filled symbols) show a good collapse, with correlation coefficients of $r^2 = 0.846$ for κ and $r^2 = 0.952$ for σ, which further establishes the agreement of our calculations and the referred experiments with known scaling relationships. The dotted lines in Figure 10(a) and (b) correspond to $(2\pi)^{-1}$ and $(4\pi)^{-1}$, respectively.

4.5. Data from tether pulling experiments may be classified according to $\mathcal{A}_{ex}$

Using a suitable choice of scaling parameters, that show a higher sensitivity to variations in the membrane excess area, data from various tether pulling assays may be classified according to the excess area in the membrane. We demonstrate this feature in Figure 11(a) where we show a plot of a vs Γ for the six model systems we have chosen. Each system is represented by a set of four data points which correspond to tethers extracted with $\mathcal{R}_{bead} = 25, 50, 75,$ and 100 nm. The entire set of data clusters into groups, that are primarily dependent only on the value of $\mathcal{A}_{ex}$ in the model membrane. It may be seen that systems M1, M3, and M5 (with $\mathcal{A}_{ex} \sim 10\%$) are clustered in the top right while M2, M4, and M6 (with $\mathcal{A}_{ex} \sim 40\%$) are clustered in the bottom left, and these two clusters are marked as shaded regions. Such a clustering analysis provides a useful route to experimentally classify cells. However, such a grouping analysis does not yield any information about the true value of $\mathcal{A}_{ex}$.

In order to obtain this information, using Equation (2), we recognize that $\mathcal{G}(\alpha)$ shows a scaling of the form G/a (dotted line in Figure 11(b)). The data from our calculations are consistent with this scaling as depicted in Figure 11(b). The data shown here despite displaying the correct scaling behavior highlight the shortcomings of existing approaches to estimate membrane excess area using Equation (2). By comparing the values of $\mathcal{A}_{ex}$ for systems M1-M6 (shown in Figure 9(a)) with the values of $\mathcal{G}(\alpha)$, it may be noted that the method based on Equation (2) consistently underpredicts the excess area for most systems (except for system M1) by nearly a factor of 5–10. This demonstration clearly supports our view as to why new analysis techniques are required to mechanotype cell membranes at the cellular scale. Given the potential for clustering of our data in Figure 11(a) on the basis of $\mathcal{A}_{ex}$, and the scaling shown in $\mathcal{G}(\alpha)$ in Figure 11(b), we define a dimensionless variable $\eta = \mathcal{A}_{ex} / \mathcal{G}$.

A plot of η as a function of a for systems M1–M6, for four different values of $\mathcal{R}_{\text{bead}}$, are shown in Figure 12(a). Intriguingly, the data collapse into a linear scaling behavior when η is plotted against a (see Figure 12(a)) where the slope of the scaling line depends only on $\mathscr{A}_{\text{ex}}$. For a given value of a, the scaling of η is represented as:

$$\eta(\mathscr{A}_{\text{ex}}) = m(\mathscr{A}_{\text{ex}})\alpha + 1, \quad (4)$$

The intercept is taken to be 1 because in the small slope limit where $\mathscr{G} \to \mathscr{A}_{\text{ex}}$ the estimation parameter $\eta(\mathscr{A}_{\text{ex}}) \to 1$. We estimate the slope $m(\mathscr{A}_{\text{ex}})$ for each system by fitting the corresponding data to a linear function. The three representative dotted lines in Figure 12(a), corresponding to the small, intermediate, and large excess area regimes, show the clustering of data that only depends on the value of $\mathscr{A}_{\text{ex}}$ in the membrane. The values of m for the six systems M1–M6 as a function of their excess area are shown in Figure 12(b). In general, the dependence of $m(\mathscr{A}_{\text{ex}})$ is unknown. As a first approximation, we find $m(\mathscr{A}_{\text{ex}})$ to be a linear function of $\mathscr{A}_{\text{ex}}$ and hence $m(\mathscr{A}_{\text{ex}}) = K\mathscr{A}_{\text{ex}}$. K being the slope of the best fit linear function, shown as a dotted line in Figure 12(b) and from our calculations we estimate its value to be 0:00085.

The presence of an excess area dependent scaling described by the slope $m(\mathscr{A}_{\text{ex}})$ in Figure 12(b) allows one to devise strategies to estimate the range of $\mathscr{A}_{\text{ex}}$ in cells directly from tether pulling experiments. One possible approach is to use self consistently solve for $\mathscr{A}_{\text{ex}}$ using the relationship:

$$\mathscr{A}_{\text{ex}} = (K\mathscr{A}_{\text{ex}}\alpha + 1)\mathscr{G}. \quad (5)$$

Here, the variables $a = \mathscr{F}_{\text{t}}\mathcal{R}_{\text{t}}/k_{\text{B}}T$ and $\mathscr{G}$ are directly computed from the tether force and radius measured in tether pulling experiments. The value of K may in turn be obtained from simulations of model systems, that correctly accounts for the size of the cytoskeletal mesh in the target cell. The excess membrane area may then be estimated by self consistently solving Equation (5).

Given the errorbars in a typical experiment, solving Equation (5) for estimating $\mathscr{A}_{\text{ex}}$ from one single measurement of $\mathscr{F}_{\text{t}}$ and $\mathcal{R}_{\text{t}}$ will not result in a robust prediction. Instead, we propose to do multiple experiments by varying $\mathcal{R}_{\text{bead}}$. For a set of N measurements, let $\mathscr{F}_{\text{t},i}$ and $\mathcal{R}_{\text{t},i}$ denote the tether force and tether radius in the ith measurement, which in turn can be used to compute a_i and $\mathscr{G}_i$. Similarly, for a chosen value of $\mathscr{A}_{\text{ex}}$ we can compute the estimation parameter for the ith measurement as $\eta_i = \mathscr{A}_{\text{ex}}/\mathscr{G}_i$. The best estimate for the excess area $\mathscr{A}_{\text{ex}}$ is obtained in an iterative manner by minimizing the objective function $\varepsilon(\mathscr{A}_{\text{ex}}) = \sum_{i=1}^{N} |(K\mathscr{A}_{\text{ex}}\alpha_i + 1) - \eta_i|^2$. This minimization procedure ensures that the best estimate of $\mathscr{A}_{\text{ex}}$ satisfies the following constraints: (i) the value of η_i follows a linear scaling, with slope a m, as in Equation (5) and (ii) the slope m has a linear dependence on $\mathscr{A}_{\text{ex}}$, as shown in Figure 12(b).

5. Discussion

We have presented a computational approach based on umbrella sampling and the weighted histogram analysis technique to compute the free energy landscape and the force-extension relationship for the pulling of membrane tethers from membrane patches of different excess membrane areas, $\mathscr{A}_{\mathrm{ex}}$. The tether forces measured in our simulations agree very well with *in vitro* tether pulling experiments on ruptured GUVs on substrate and on HeLa cells. Unlike existing models, we are able to account for both mechanical work as well as entropic work in tether extraction by performing finite temperature calculations, delineation of the Helmholtz free energy, and performing the analysis in an ensemble with non-zero $\mathscr{A}_{\mathrm{ex}}$. In the tether formation regime, based on the computed values of the force required for tether extraction and the tether radius, we established scaling relationships involving $\mathscr{F}_{\mathrm{t}}$, $\mathscr{R}_{\mathrm{t}}$, and $\mathscr{A}_{\mathrm{ex}}$. We demonstrated the relevance of the calculations by showing the scaling of κ with a and σ with Γ from the model and those obtained from 15 different cell experiments collapse on to a single curve. These scaling curves can be used to construct new schemes for estimating the excess membrane area, which alleviate the limitations of previous methods by being valid for large curvatures, and by taking into account the thermal membrane undulations in the high curvature limit. We have shown that our results successfully recapitulate the results of the previous model in the small-curvature limit. However, in the large-curvature limit, when the domain of applicability of the previous model is limited, we predict the values of the excess membrane areas that are substantially larger than the estimates from the small-curvature model. In light of the discussion above, there is a profound biomedical ramification of the excess membrane area distribution as revealed by our analyses of the tether pulling experiments using the fully non-linear model of the membrane patch subject to finite temperature undulations.

Our model while directly relevant to tether extraction in well behaved *in vitro* setups, such as GUVs or supported bilayers, does not include the full complexity required to recapitulate the cellular experiments. The complexities arise due to: (i) the dynamic nature of the cytoskeletal reorganization, (ii) changes in $\mathscr{A}_{\mathrm{ex}}$ due to cellular trafficking mechanisms; the latter poses an important constraint regarding the ensemble. While in *in vitro* experiments or in our model, we have the ability to either select/design a constant $\mathscr{A}_{\mathrm{ex}}$ or a constant σ ensemble, it is not obvious what the correct cellular condition would be. For example, at early timescales (i.e. too short for changes in l_c) the cell membrane patch may be under a state of tension but at later times both σ and $\mathscr{A}_{\mathrm{ex}}$ can change due to signaling and trafficking. Notwithstanding these considerations, our model can still be applicable under certain cellular conditions, namely (i) the timescale of the tether extraction is faster than that for cytoskeletal reorganization and trafficking (~ 10-100 s [57]); (ii) the dimensions of the extracted tethers are smaller than l_c. When these conditions are met, one can treat the tether extraction as a quasi-equilibrium process where the cytoskeleton merely serves as a pinning boundary condition for the membrane. This is further justified because the membrane tension equilibrates at a much faster time scale of $\tau_{\mathrm{tension}} = \eta_s \sigma \sim 1$-$100 \mu s$, (where η_s is the surface dilational viscosity of the bilayer ≈ 0.35 Ns/m [58]). Under these assumptions, $\mathscr{L}_{\mathrm{patch}}$ can serve as an approximate surrogate to include cytoskeletal pinning effects. These

considerations and caveats must be taken into consideration in developing experimental methods for determining $\mathscr{A}_{\mathrm{ex}}$ in cells based on the model we have described here.

From a broader perspective, the geometric characterization of cell membrane excess area, the main topic of discussion in this article, is important in circumstances where the cell membrane plays a dominant role such as in the viral invasion of host cells in virology, formation of the immunological synapse in adaptive immunity, or targeted delivery of nanocarriers in pharmacology. It is also expected to be crucial in circumstances where the underlying heterogeneity is intrinsic such as in a tumor microenvironment as it influences cell fate through outside-in mechanisms relayed via membrane mechanotransduction to intracellular signaling.

Supplementary Material

Refer to Web version on PubMed Central for supplementary material.

Acknowledgments

References

1. Suresh S. Acta Biomater. 2007; 3:413–438. [PubMed: 17540628]

2. Physical Sciences - Oncology Centers Network. Agus DB, Alexander JF, Arap W, Ashili S, Aslan JE, Austin RH, Backman V, Bethel KJ, Bonneau R, Chen WC, Chen-Tanyolac C, Choi NC, Curley SA, Dallas M, Damania D, Davies PCW, Decuzzi P, Dickinson L, Estevez-Salmeron L, Estrella V, Ferrari M, Fischbach C, Foo J, Fraley SI, Frantz C, Fuhrmann A, Gascard P, Gatenby RA, Geng Y, Gerecht S, Gillies RJ, Godin B, Grady WM, Greenfield A, Hemphill C, Hempstead BL, Hielscher A, Hillis WD, Holland EC, Ibrahim-Hashim A, Jacks T, Johnson RH, Joo A, Katz JE, Kelbauskas L, Kesselman C, King MR, Konstantopoulos K, Kraning-Rush CM, Kuhn P, Kung K, Kwee B, Lakins JN, Lambert G, Liao D, Licht JD, Liphardt JT, Liu L, Lloyd MC, Lyubimova A, Mallick P, Marko J, McCarty OJT, Meldrum DR, Michor F, Mumenthaler SM, Nandakumar V, O'Halloran TV, Oh S, Pasqualini R, Paszek MJ, Philips KG, Poultney CS, Rana K, Reinhart-King CA, Ros R, Semenza GL, Senechal P, Shuler ML, Srinivasan S, Staunton JR, Stypula Y, Subramanian H, Tlsty TD, Tormoen GW, Tseng Y, van Oudenaarden A, Verbridge SS, Wan JC, Weaver VM, Widom J, Will C, Wirtz D, Wojtkowiak J, Wu PH. Sci Rep. 2013; 3:1449. [PubMed: 23618955]

3. Steward RL, Rosner SR, Zhou EH, Fredberg JJ. Swiss Med Wkly. 2013; 143:w13766. [PubMed: 23519500]

4. Lee GYH, Lim CT. Trends Biotechnol. 2007; 25:111–118. [PubMed: 17257698]

5. Van Vliet KJ, Bao G, Suresh S. Acta Materialia. 2003; 51:5881–5905.

6. Sheetz MP, Sable JE, Döbereiner HG. Annu Rev Biophys Biomol Struct. 2006; 35:417–434. [PubMed: 16689643]

7. Acerbi I, Cassereau L, Dean I, Shi Q, Au A, Park C, Chen YY, Liphardt J, Hwang ES, Weaver VM. Integr Biol. 2015; 7:1120–1134.

8. Diz-Muñoz A, Fletcher DA, Weiner OD. Trends in Cell Biology. 2013; 23:47–53. [PubMed: 23122885]

9. Mih JD, Marinkovic A, Liu F, Sharif AS, Tschumperlin DJ. Journal of Cell Science. 2012; 125:5974–5983. [PubMed: 23097048]

10. Paszek MJ, Zahir N, Johnson KR, Lakins JN, Rozenberg GI, Gefen A, Reinhart-King CA, Margulies SS, Dembo M, Boettiger D, Hammer DA, Weaver VM. Cancer Cell. 2005; 8:241–254. [PubMed: 16169468]

11. Samuel MS, Lopez JI, McGhee EJ, Croft DR, Strachan D, Timpson P, Munro J, Schröder E, Zhou J, Brunton VG, Barker N, Clevers H, Sansom OJ, Anderson KI, Weaver VM, Olson MF. Cancer Cell. 2011; 19:776–791. [PubMed: 21665151]

12. Paszek MJ, DuFort CC, Rossier O, Bainer R, Mouw JK, Godula K, Hudak JE, Lakins JN, Wijekoon AC, Cassereau L, Rubashkin MG, Magbanua MJ, Thorn KS, Davidson MW, Rugo HS, Park JW, Hammer DA, Giannone G, Bertozzi CR, Weaver VM. Nature. 2014; 511:319–325. [PubMed: 25030168]

13. Zuo X, Zhang J, Zhang Y, Hsu SC, Zhou D, Guo W. Nature Cell Biology. 2006; 8:1383–1388. [PubMed: 17086175]

14. Zhao Y, Liu J, Yang C, Capraro BR, Baumgart T, Bradley RP, Ramakrishnan N, Xu X, Radhakrishnan R, Svitkina T, Guo W. Developmental Cell. 2013; 26:266–278. [PubMed: 23948253]

15. Ritchie K, Iino R, Fujiwara T, Murase K, Kusumi A. Mol Membr Biol. 2003; 20:13–18. [PubMed: 12745919]

16. Morone N, Fujiwara T, Murase K, Kasai RS, Ike H, Yuasa S, Usukura J, Kusumi A. The Journal of Cell Biology. 2006; 174:851–862. [PubMed: 16954349]

17. Sens P, Plastino J. J Phys: Condens Matter. 2015; 27

18. McMahon HT, Gallop JL. Nature Cell Biology. 2005; 438:590–596.

19. Zimmerberg J, Kozlov MM. Nat Rev Mol Cell Biol. 2006; 7:9–19. [PubMed: 16365634]

20. Goh LK, Sorkin A. Cold Spring Harbor Perspectives in Biology. 2013; 5:a017459–a017459. [PubMed: 23637288]

21. Grant BD, Donaldson JG. Nat Rev Mol Cell Biol. 2009; 10:597–608. [PubMed: 19696797]

22. Bryant DM, Mostov KE. Nat Rev Mol Cell Biol. 2008; 9:887–901. [PubMed: 18946477]

23. Orlando K, Guo W. Cold Spring Harbor Perspectives in Biology. 2009; 1:a001321. [PubMed: 20066116]

24. Luo T, Mohan K, Iglesias PA, Robinson DN. Nature Materials. 2013; 12:1064–1071. [PubMed: 24141449]

25. Sheetz MP. Nat Rev Mol Cell Biol. 2001; 2:392–396. [PubMed: 11331914]

26. Miaczynska M. Cold Spring Harbor Perspectives in Biology. 2013; 5:a009035. [PubMed: 24186066]

27. Schmid-Schönbein GW, Shih YY, Chien S. Blood. 1980; 56:866–875. [PubMed: 6775712]

28. Bo L, Waugh RE. Biophys J. 1989; 55:509–517. [PubMed: 2930831]

29. Hochmuth FM, Shao JY, Dai J, Sheetz MP. Biophys J. 1996; 70:358–369. [PubMed: 8770212]

30. Jiang YQ, Guo HL, Liu CX, Li ZL, Cheng BY, Zhang DZ, Jia ST. Chinese Physics Letters. 2004; 21:1659–1662.

31. Derényi I, Jülicher F, Prost J. Phys Rev Lett. 2002; 88:238101. [PubMed: 12059401]

32. Powers T, Huber G, Goldstein R. Phys Rev E. 2002; 65:041901.

33. Schumacher KR, Popel AS, Anvari B, Brownell WE, Spector AA. Phys Rev E. 2009; 80:041905.

34. Brownell WE, Qian F, Anvari B. Biophys J. 2010; 99:845–852. [PubMed: 20682262]

35. Khatibzadeh N, Gupta S, Farrell B, Brownell WE, Anvari B. Soft Matter. 2012; 8:8350. [PubMed: 23227105]

36. Ramakrishnan N, Tourdot RW, Eckmann DM, Ayyaswamy PS, Muzykantov V, Radhakrishanan R. J Royal Society Open Science. 2016; 3:160260.

37. Baumgärtner A, Ho J. Phys Rev A. 1990; 41:5747–5750. [PubMed: 9902972]

38. Kroll DM, Gompper G. Science. 1992; 255:968–971. [PubMed: 1546294]

39. Canham P B. J Theor Biol. 1970; 26:61–81. [PubMed: 5411112]

40. Helfrich W. Z Naturforsch C. 1973; 28:693. [PubMed: 4273690]

41. Ramakrishnan N, Sunil Kumar PB, Ipsen JH. Phys Rev E. 2010; 81:041922.

42. Tourdot RW, Ramakrishnan N, Radhakrishnan R. Phys Rev E. 2014; 90:022717.

43. Shiba H, Noguchi H, Fournier JB. Soft Matter. 2016; 12:2373–2380. [PubMed: 26796575]

44. Metropolis N, Rosenbluth AW, Rosenbluth MN, Teller AH, Teller E. J Chem Phys. 1953; 21:1087–1092.

45. Helfrich W, Servuss RM. Il Nuovo Cimento D. 1984; 3:137–151.

46. Waheed Q, Edholm O. Biophys J. 2009; 97:2754–2760. [PubMed: 19917229]

47. Phillips, R., Kondev, J., Theriot, J. Physical biology of the cell. Garland Science; 2009.

48. Frenkel, D., Smit, B. Understanding Molecular Simulation : From Algorithms to Applications. 2nd. Academic Press; 2001.

49. Kumar S, Rosenberg JM, Bouzida D, Swendsen RH, Kollman PA. J Comput Chem. 1992; 13:1011–1021.

50. Roux B. Computer Physics Communications. 1995; 91:275–282.

51. Weinberger A, Tsai FC, Koenderink GH, Schmidt TF, Itri R, Meier W, Schmatko T, Schröder A, Marques C. Biophys J. 2013; 105:154–164. [PubMed: 23823234]

52. Hutter JL, Bechhoefer J. Review of Scientific Instruments. 1993; 64:1868–1873.

53. Singh P, Mahata P, Baumgart T, Das SL. Phys Rev E. 2012; 85:051906.

54. Lipowsky R. Nature. 1991; 349:475–481. [PubMed: 1992351]

55. Seifert U. Advances in Physics. 1997; 46:13–137.

56. Pontes B, Ayala Y, Fonseca ACC, Romão LF, Amaral RF, Salgado LT, Lima FR, Farina M, Viana NB, Moura-Neto V, Nussenzveig HM. PLoS ONE. 2013; 8:e67708. [PubMed: 23844071]

57. Joanny JF, Prost J. HFSP journal. 2009; 3:94–104. [PubMed: 19794818]

58. Haluska CK, Riske KA, Marchi-Artzner V, Lehn JM, Lipowsky R, Dimova R. Proc Natl Acad Sci USA. 2006; 103:15841–15846. [PubMed: 17043227]
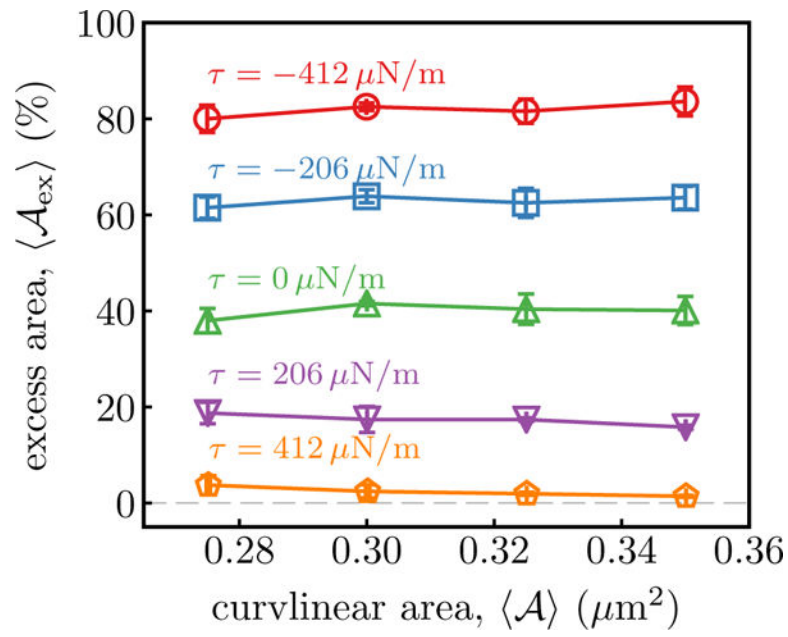
Figure 1.
Equilibrium values of $\langle \mathscr{A}_{ex} \rangle$ as a function of $\langle \mathscr{A} \rangle$ in the constant N-σ-τ-T ensemble. Data shown for five different values of τ=−412, −206, 0, 206 and 412 μN/m, for a membrane with $\kappa = 20\ k_B T$ and $\sigma = 0$.
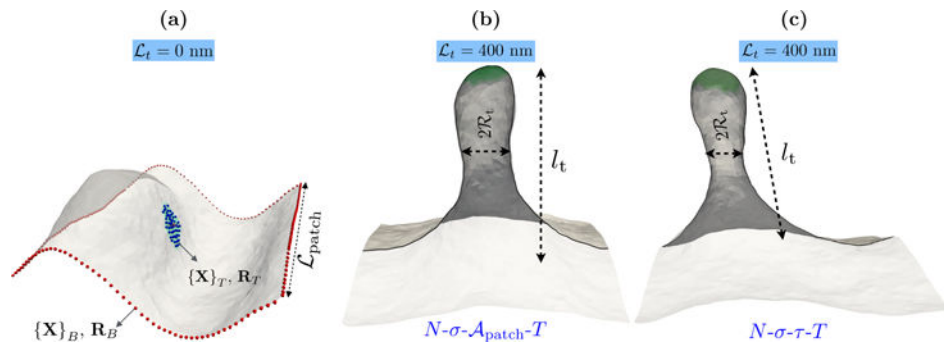
Figure 2.
(a) Representative equilibrium conformation of a membrane with $\kappa = 20$ $k_\mathrm{B} T$ and $\mathscr{A}_\mathrm{ex} \sim 40\%$. The set of biased vertices at the tip ($\{\mathbf{X}_T\}$) and at the base ($\{\mathbf{X}_B\}$) are explicitly marked as spheres — $\mathbf{R}_T$ and $\mathbf{R}_B$ denote their respective center of masses. $\{\mathbf{X}_T\}$ is the set of all vertices within a region of size $\mathscr{R}_\mathrm{bead}$. The conformation of the membrane with a fully developed tether for $\mathscr{L}_\mathrm{t}$=400 nm are shown in panels (b) and (c). The snapshot in panel (b) corresponds to a constant $N-\sigma-\mathscr{A}_\mathrm{patch}-T$ ensemble, while that in (c) corresponds to a constant $N\text{-}\sigma\text{-}\tau\text{-}T$ ensemble. l_t and $\mathscr{R}_\mathrm{t}$, the length and radius of the membrane tether, and the membrane dimension $\mathscr{L}_\mathrm{patch}$ are also marked.
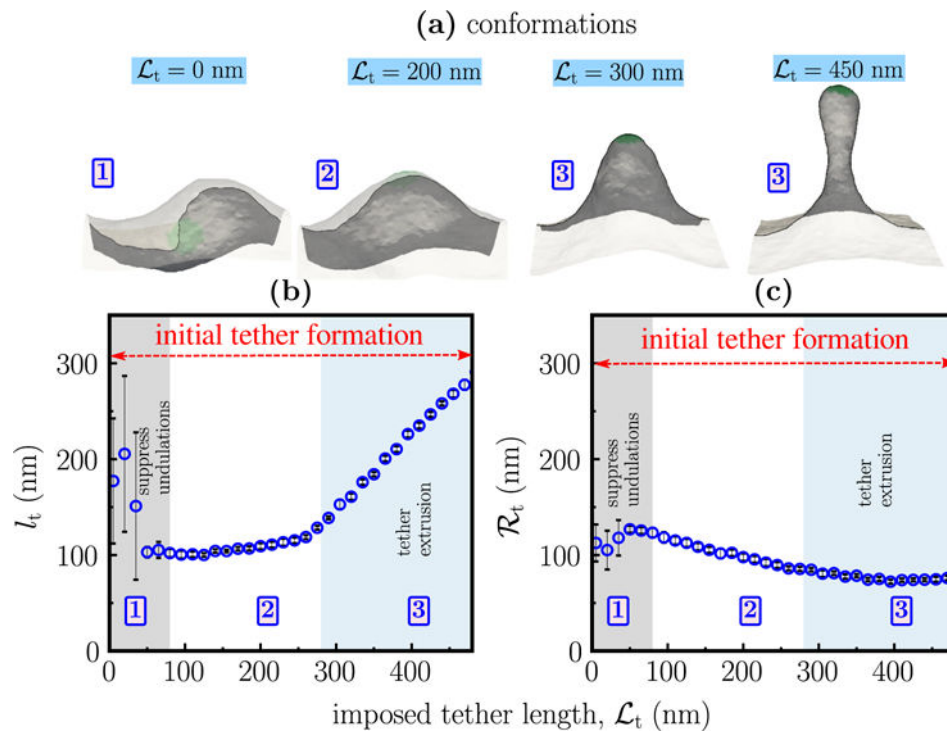
Figure 3.
(a) Representative conformations of a membrane with $\kappa = 20\ k_B T$ and $\mathscr{A}_{ex} \sim 40\%$ as a function of $\mathcal{L}_t$. Panels (b) and (c) show the computed values of the tether length l_t, and radius $\mathcal{R}_t$, respectively, as a function of $\mathcal{L}_t$. These quantities are computed as described in the methods section. The shaded regions mark the three regimes for initial tether formation (i.e., for $l_t/\mathcal{R}_t < 5$) namely, regime **1**: suppression of undulations, regime **2**: formation of tethers, and regime **3**: extrusion of tethers at a constant radius. The boxed numbers in the top panel denote the regimes to which the configurations correspond to.
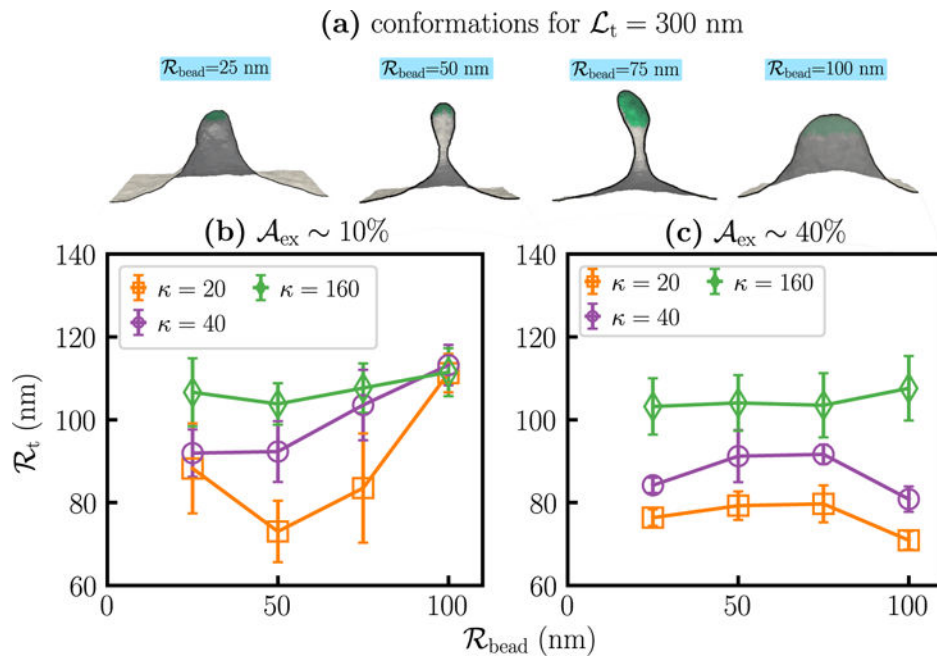
Figure 4.
Dependence of the tether radius on the size of the biasing region. (a) Representative conformations of tethers, for $\mathcal{L}_t$=300 nm, extracted using beads with $\mathcal{R}_{bead}$ = 25, 50, 75, and 100 nm, from a membrane with κ = 20 $k_B T$ and $\mathcal{A}_{ex}\sim10\%$. Panels (b) and (c) show the computed values of $\mathcal{R}_t$, as a function of $\mathcal{R}_{bead}$, for κ = 20, 40, and 160 $k_B T$ for $\mathcal{A}_{ex}$=10 and 40%, respectively.
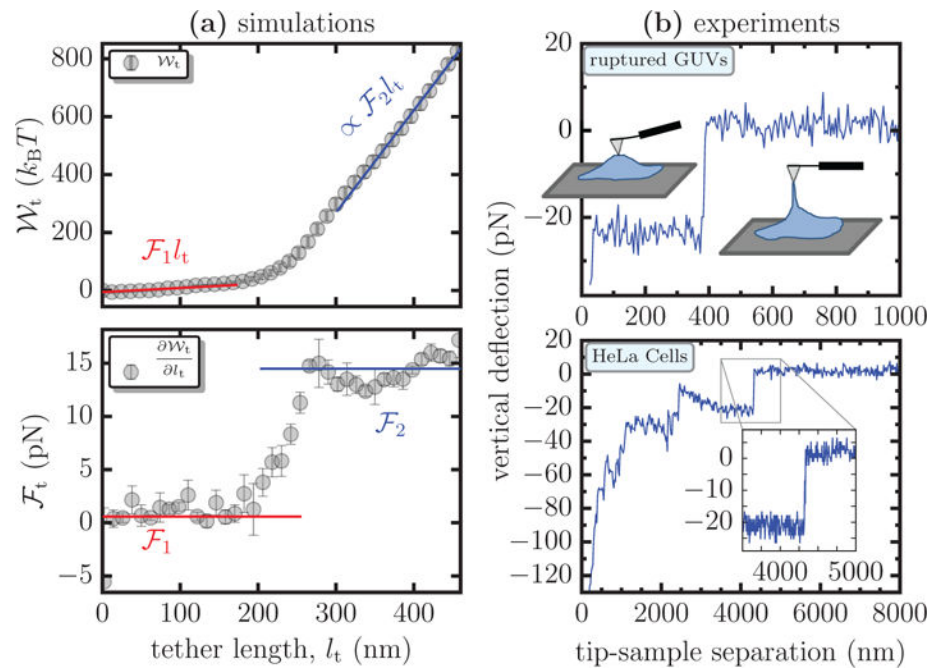
Figure 5.
(a) The potential of mean force $\mathscr{W}_t$ and the tether force $\mathscr{F}_t$, as a function of the tether length l_t, for a membrane with $\kappa = 20$ $k_B T$ and $\mathscr{A}_{ex} \sim 40\%$. In the top panel, $\mathscr{W}_t$ shows a linear scaling in regimes 1 and 3, which are represented by the functions $\mathscr{F}_1 l_t$ and $\mathscr{F}_2 l_t$, respectively. The lower panel compares values of $\mathscr{F}_t$ estimated from direct numerical differentiation of $\mathscr{W}_t$ (symbols) to that obtained from the scaling relations (lines). (b) Force displacement curves for experimental tether pulling assay using ruptured GUVs (top panel) and HeLa cells (lower panel) – the inset shows a transition between regions of constant force. The illustration in the top panel shows the state of the membrane tether at various stages of the experiment. The vertical deflection of the AFM tip is measure of the tether force $\mathscr{F}_t$ and its separation from the sample is a measure of the tether length l_t.
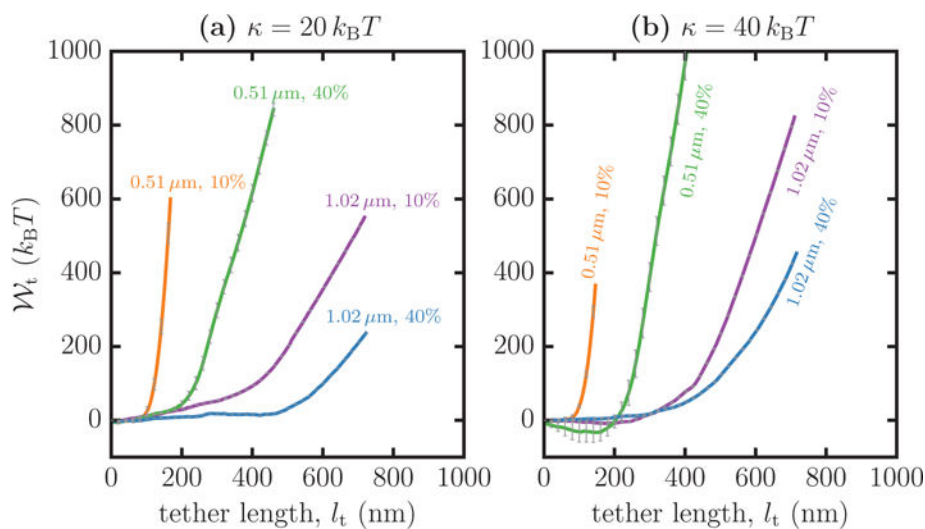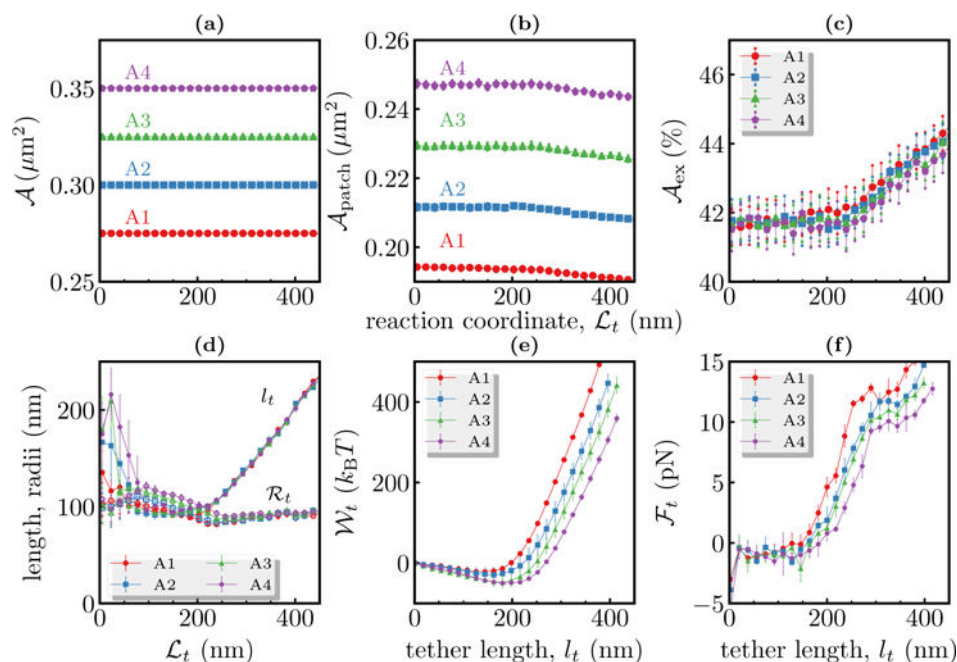
Figure 6.
The potential of mean force $\mathcal{W}_t$ as a function of the tether length l_t, extracted with $\mathcal{R}_{bead} =$ 50 nm, from membranes with $\mathcal{L}_{patch} = 0.51\ \mu$m and $1.02\ \mu$m, and excess areas $\mathcal{A}_{ex} = 10\%$ and 40%. Data for $\kappa = 20\ k_BT$ are shown in panel (a) and that for $\kappa = 40\ k_BT$ is shown in panel (b).

Figure 7.

Comparison of tether characteristics in the constant N-σ-τ-T ensemble for four different membrane patches, denoted A1-A4. Panels (a), (b) and (c) show the area $(\mathscr{A})$, projected area $(\mathscr{A}_{\text{patch}})$ and excess area $(\mathscr{A}_{\text{ex}})$ as a function of the reaction coordinate $\mathcal{L}_t$. The measured values of tether length l_t and tether radius $\mathcal{R}_t$ are shown in panel (d) as filled and open symbols, respectively. The potential of mean forces and the tether forces are shown in panels (e) and (f) as a function of the tether length l_t.
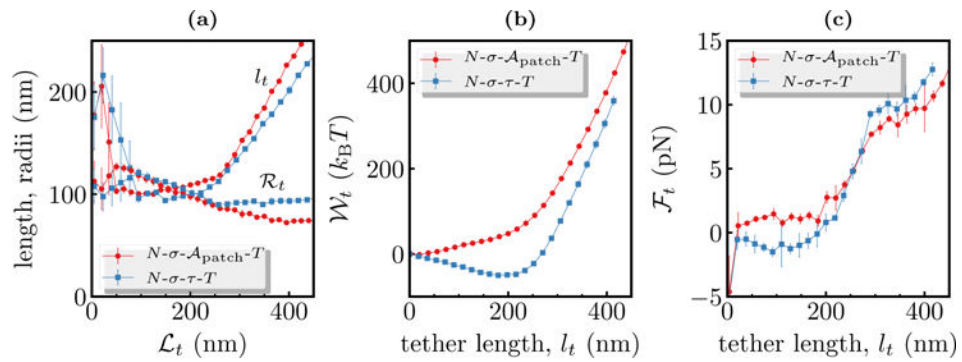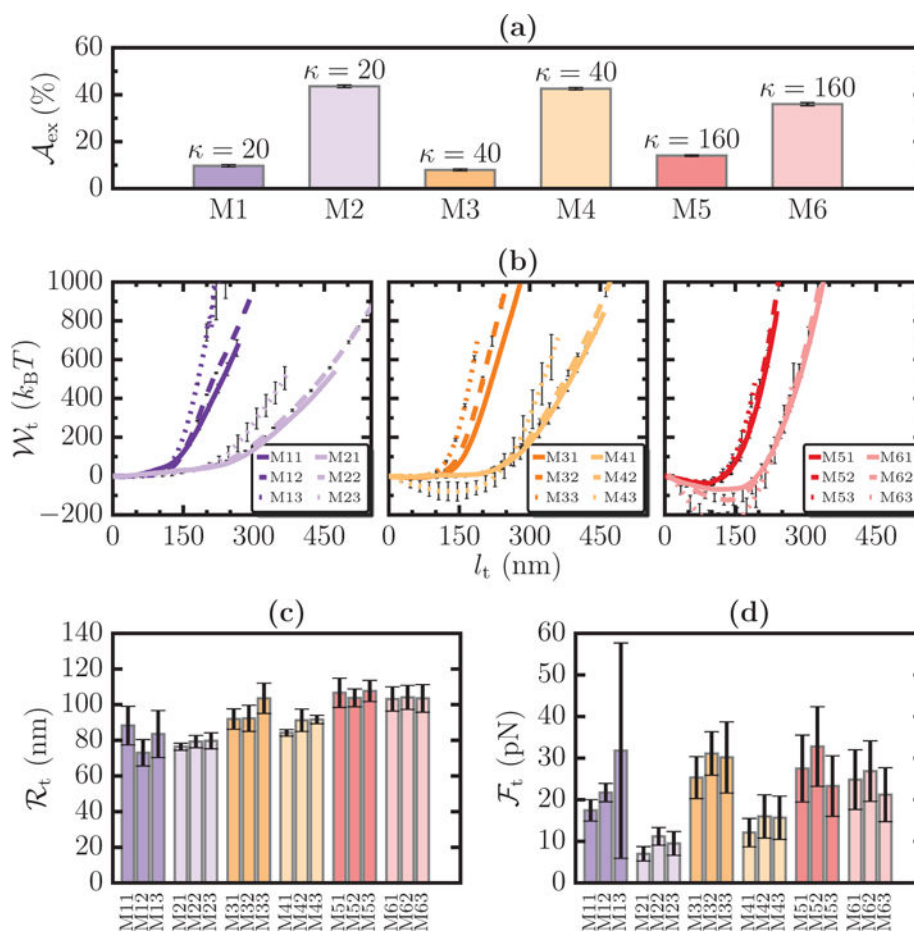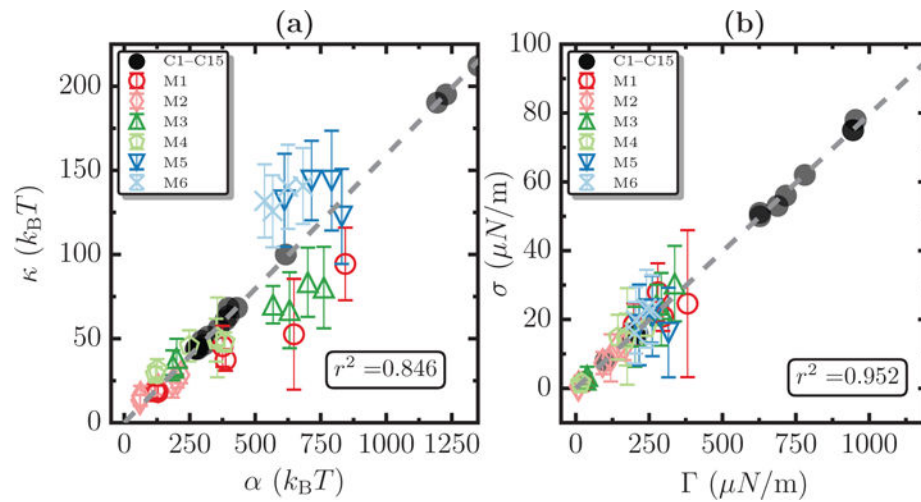
Figure 8.

Comparison of tether characteristics in the constant $N-\sigma-\mathscr{A}_{\mathrm{patch}}-T$ and N-σ-τ-T ensembles. In panel (a), the tether length and radius are shown as open and filled symbols, respectively. The potential of mean forces (panel (e)) and tether force (panel (f)) are plotted as a function of the tether length l_t. Data shown for a membrane with $\kappa = 20$ $k_B T$.

Figure 9.
(a) Six model membrane systems, denoted M1–M6, with specified values of $\mathscr{A}_{\text{ex}}$ and κ. For any system $M_i\,(i = 1 \cdots 6)$, M_{i1}, M_{i2}, and M_{i3} correspond to tethers extracted with $\mathscr{R}_{\text{bead}} = 25$, 50, and 75 nm, respectively. The values of $\mathscr{W}_{\text{t}}$, $\mathscr{F}_{\text{t}}$, and $\mathscr{R}_{\text{t}}$ for all the systems are shown in panels (b), (c), and (d), respectively.

Figure 10.
Validity of the scaling relations for κ and σ for data from simulations (M1–M6, shown as open symbols) and experiments (C1–C15, shown as filled symbols). Panel (a) shows the relation $\kappa/\alpha = 1/2\pi$ and panel (b) shows the scaling relation $\sigma/\Gamma = 1/4\pi$, and the corresponding correlation coefficients for systems M1-M6 are found to be $r^2 = 0.846$ and $r^2 = 0.952$, respectively. The dotted lines in panels (a) and (b) correspond to $1/2\pi$ and $1/4\pi$ respectively.
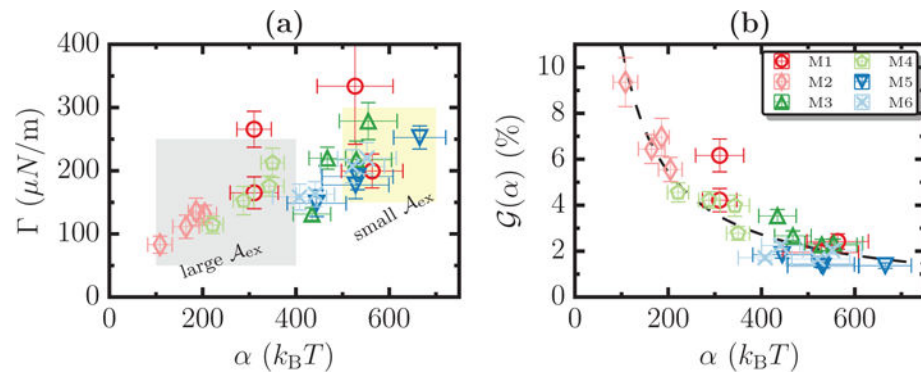
Figure 11.
(a) A plot of α vs Γ for M1–M6, for different values of $\mathcal{R}_{bead}$, show data clustering in an excess area dependent fashion. (b) $\mathcal{G}(\alpha)$, the analytical estimates for the membrane excess area for M1–M6, computed using Equation (2). The dotted line denotes a scaling of the form G/a, with $G \sim 1107$.
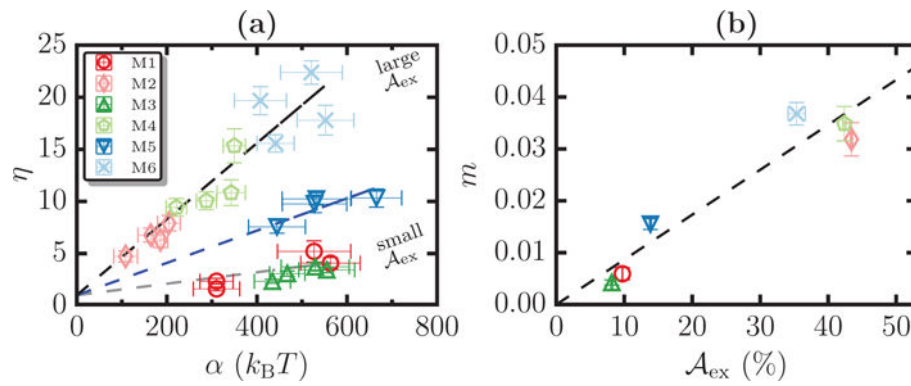
Figure 12.
(a) Scaling plot of η vs a for systems M1–M6 for four different values of $\mathscr{R}_{bead}$. The dotted lines, show representative scaling relations of the form $\eta = ma + 1$, for small, intermediate, and large $\mathscr{A}_{ex}$ regimes. (b) A plot of the slope m as a function of $\mathscr{A}_{ex}$ and the dotted lines denote the best linear fit to the data. Fitting $m(\mathscr{A}_{ex}) = K\mathscr{A}_{ex}$ we find the value of $K = 0.00085$.